applied sciences

Article

Newly Designed Identification Scheme for Monitoring Ice Thickness on Power Transmission Lines

Nalini Rizkyta Nusantika, Xiaoguang Hu and Jin Xiao *

State Key Laboratory of Virtual Reality Technology and Systems, School of Automation Science and Electrical Engineering, Beihang University, Beijing 100191, China; nusantikanalini@buaa.edu.cn (N.R.N.); xiaoguang@buaa.edu.cn (X.H.)
* Correspondence: xiaojin_ck@126.com; Tel.: +86-10-82339780

Abstract: Overhead power transmission line icing (PTLI) disasters are one of the most severe dangers to power grid safety. Automatic iced transmission line identification is critical in various fields. However, existing methods primarily focus on the linear characteristics of transmission lines, employing a two-step process involving edge and line detection for PTLI identification. Nonetheless, these traditional methods are often complicated when confronted with challenges such as background noise or variations in illumination, leading to incomplete identification of the target area, missed target regions, or misclassification of background pixels as foreground. This paper proposes a new iced transmission line identification scheme to overcome this limitation. In the initial stage, we integrate the image restoration method with image filter enhancement to restore the image's color information. This combined approach effectively retains valuable information and preserves the original image quality, thereby mitigating the noise presented during the image acquisition. Subsequently, in the second stage, we introduce an enhanced multi-threshold algorithm to separate background and target pixels. After image segmentation, we enhance the image and obtain the region of interest (ROI) through connected component labeling modification and mathematical morphology operations, eliminating background regions. Our proposed scheme achieves an accuracy value of 97.72%, a precision value of 96.24%, a recall value of 86.22%, and a specificity value of 99.48% based on the average value of test images. Through object segmentation and location, the proposed method can avoid background interference, effectively solve the problem of transmission line icing identification, and achieve 90% measurement accuracy compared to manual measurement on the collected PTLI dataset.

Keywords: power transmission line icing; icing thickness; transmission line identification; multi-threshold; image restoration; connected component labeling

check for updates

Citation: Nusantika, N.R.; Hu, X.; Xiao, J. Newly Designed Identification Scheme for Monitoring Ice Thickness on Power Transmission Lines. *Appl. Sci.* **2023**, *13*, 9862. https://doi.org/10.3390/app13179862

Academic Editors: Andrea Prati, Bruno Fernandes and Rogério Pontes

Received: 12 July 2023
Revised: 24 August 2023
Accepted: 29 August 2023
Published: 31 August 2023

1. Introduction

The development of the intelligent grid has increased the design, operation, and maintenance requirements for power transmission lines. Additionally, transmission lines are susceptible to icing at low temperatures, high air humidity, and precipitation [1–6]. The first accident caused by icing on overhead transmission lines in human history occurred in the United States in 1932 [7]. Following the disaster, ice damage to transmission lines occurred in Britain in 1935 and 1962. Between 1980 and 2000, icing disasters happened on transmission lines. Snow and ice caused power transmission line failures in Ohio, Chicago, and Idaho, as well as Quebec and Ontario in Canada, Russia, Norway, Yugoslavia, Japan, the United Kingdom, Sweden, Finland, and Iceland [8]. Since the beginning of the twenty-first century, severe icing disasters on power transmission lines have happened in the Czech Republic, Alberta, and Canada. In 2005 and 2008, significant ice and snow disasters occurred in southern China. More than 36,000 transmission lines were broken, many electric towers collapsed, and many areas had continuous power outages, disrupting the power supply for more than 27 million households [9]. In February 2021, an icing disaster happened on the electrical grid in Texas, USA, leaving millions of people without power in the cold weather [10]. Therefore, an effective monitoring and predictive alarm system for power transmission line icing (PTLI) is important for ensuring the safety of the power grid.

Traditional PTLI monitoring techniques, such as artificial inspection [11], the installation of pressure sensors [12], and the development of meteorological models [13], among others, have been extensively employed to achieve this objective. In recent years, PTLI monitoring based on computer vision methods has emerged as a new research direction [14] that makes ice monitoring easier and more practical and cost-effective. Several 2D algorithms, such as adaptive threshold segmentation [15], edge extraction [16], and wavelet analysis [17], are presented to obtain accurate ice edge information. The ice thickness can be calculated by comparing the pixel dimensions between edges in normal and icy conditions. However, these algorithms perform poorly in complex contexts or situations with limited exposure. Furthermore, the 2D estimation method cannot obtain comprehensive information about ice thickness. Methods based on 3D measurement have been introduced to better monitor PTLI and obtain more accurate information to address this issue. The PTLI monitoring based on 3D monitoring mainly includes camera calibration, transmission line identification, key point matching, and ice thickness calculation.

The identification of iced transmission lines is an important part of PTLI monitoring. At this stage, the goal is to identify the top and bottom of the iced transmission line because it will directly affect the ice thickness measurement. Generally, the iced transmission line identification stage consists of two parts, namely edge detection and line detection. Edge detection accuracy is related to low contrast, cluttered backgrounds, occlusion, and the image quality obtained by the camera [18]. Noise in PTLI scene images is typically introduced during image acquisition or transmission. Environmental conditions during image acquisition and insufficient light levels may introduce noise in the image, which can significantly affect the quality of the captured image. Environmental conditions such as particles or smudges on the lens can also result in distorted or blurry images. Subsequently, noise due to variations in illumination conditions such as brightness, contrast, and color temperature can result in a loss of image quality and affect the accuracy of any analysis or interpretation performed on the image. Additionally, inadequate light levels can lead to underexposed images, making it challenging to capture important details and reducing overall visibility [19,20]. Based on the above reasons, finding an accurate edge detection method for iced transmission line identification is crucial. According to previous researchers, conventional edge detection operators have categories, such as first-order derivative or gradient-based [21]. Traditional edge detection methods use low-level signs such as colors, brightness, textures, and gradients in the images [22]. However, there is a need for more accuracy to meet the application requirements. Traditional Canny and Hough transforms have often been applied to identify line icing [6], with Canny operators for edge detection of line icing and Hough transforms for straight lines [23,24]. However, this method has interference noise, so other objects are sometimes detected. The lighting in the image also has a significant impact on this conventional edge detection [3]. The Canny edge detection algorithm has a few things to improve, such as fracture edges [25,26]. Many edges of objects in the background are also detected, making it challenging to distinguish which object (the iced transmission line) is selected and which is in the background. Zhang et al. [18] proposed an edge detection algorithm for images of iced transmission lines based on wavelet transform and morphology fusion to keep image background and noise from disrupting the edge detection identification result.

Based on the problems above, the main works and innovations proposed in this paper include:

- An image optimization method that combines the image restoration method and image filter enhancement to alleviate the influence of noise and light on iced transmission line detection.

- An enhanced multi-level threshold algorithm to segment background and target pixel areas.
- A connected component labeling modification and mathematical morphological operations to refine the segmentation image, obtain the ROI, and determine the position of the top and bottom of the line.

This paper is organized as follows: Section 2 summarizes PTLI identification and extraction. Section 3 illustrates the proposed method for transmission line icing identification. Section 4 introduces our proposed ice thickness calculation using 3D measurements. Section 5 presents the experimental results and discussion, and Section 6 states the conclusions and future work.

2. Transmission Line Icing Identification

The main problem in PTLI monitoring based on binocular vision is identifying and extracting iced transmission lines, directly affecting monitoring automation and intelligence. The target detection algorithm identifies and extracts the image of iced transmission lines. When identifying PTLI, the accuracy of edge and line detection algorithms using traditional methods still needs to be improved, and noise interference from PTLI images is quite large. The high similarity in color and texture makes their detection and identification more difficult. Generally, PTLI identification uses the Canny algorithm to detect the edges of iced lines [23,24], but the result has fractured edges and free points. Identifying PTLI with traditional methods is also not optimal for eliminating background noise and detecting iced lines in dim areas. Therefore, designing a reliable scheme for identifying iced transmission lines is crucial. Table 1 shows the shortcomings of identification methods in previous studies for PTLI scenes. Figure 1 shows the results of PTLI identification using Canny edge detection and the Hough transform. Based on Figure 1, there are areas with fractured edges, and the Hough transform is not optimal for detecting the whole line in the icing line area.

Table 1. The shortcomings of the previous method for edge detection of PTLI images.

No.	Original Image	Result	Problem
1	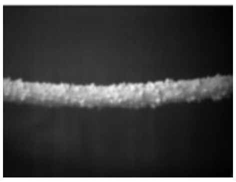	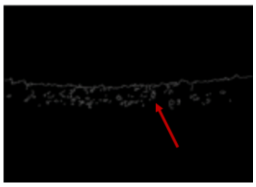	Fracture edge and free point
2	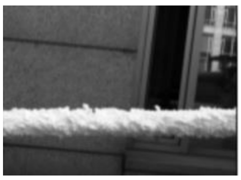	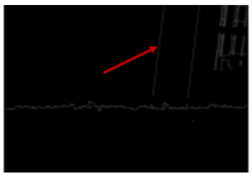	Background interference
3		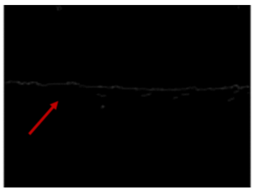	Dim areas are not detected by traditional methods

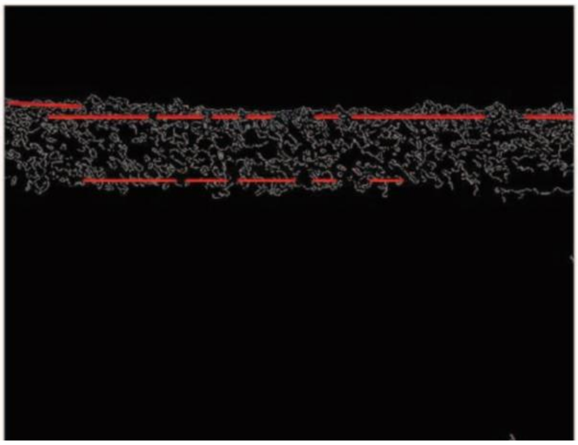

Figure 1. The PTLI identification uses Canny edge detection and the Hough transform.

3. New Scheme for Iced Transmission Line Identification

This paper proposes a reliable iced transmission line identification scheme to overcome difficulties with PTLI identification. Figure 2 shows our proposed scheme for iced transmission line identification. We integrate image restoration techniques with image filter enhancements in the early stages. This stage solves problems such as increased noise in the original image, dim and dark images, and a grayish tint in the original image. In addition, image filter enhancement is proposed to remove unwanted noise during image acquisition and retain valuable information, such as the edges of the transmission line and the texture of the iced lines. PTLI images often blend with other objects, or noise appears during image processing even though the background is simple. Therefore, the next stage is an enhanced multi-level segmentation threshold algorithm to segment background and target pixel areas. The results of multi-level threshold images contain gaps and holes, so morphological modification operations are performed to improve segmentation results by utilizing two multiscale and mathematically structuring elements. We enhance the image and obtain the region of interest (ROI) based on bounding box identification to eliminate background regions. After object segmentation and localization, the next step is PTLI edge identification. Mathematical morphology is proposed at this stage to extract multidirectional edge subplots and smooth the region. Finally, modified connected component labeling is proposed to identify the top and bottom of the iced lines. This modification reduces the processing time and memory space required to analyze neighboring pixels. A more detailed explanation of the stages in iced transmission line identification is explained in the sub-section below. The black arrows in Figure 2 show the flow of identifying and extracting iced transmission lines. The red arrows explain the process in detail at these stages.

3.1. Image Color Restoration

The material images taken by cameras often appear dim and unclear, and distorted hues alter their true colors. Likewise, the appearance of color in recorded images is strongly influenced by spectral shifts in the scene illumination. The reason has two parts: insufficient light prevents the camera from gathering enough information, and the dynamic range of a camera is much narrower than that of the human visual system. Some of the iced transmission line images used in this study appear dim and unclear, and distorted hues have altered their original color, so restoring the original image before going to the next stage is needed. Retinex (Retina + Cortex) is an enhancement technique that attempts to attain color constancy and is used to enhance the image's color. Figure 3 shows a block diagram for image color restoration, and Algorithm 1 shows the color restoration algorithm.

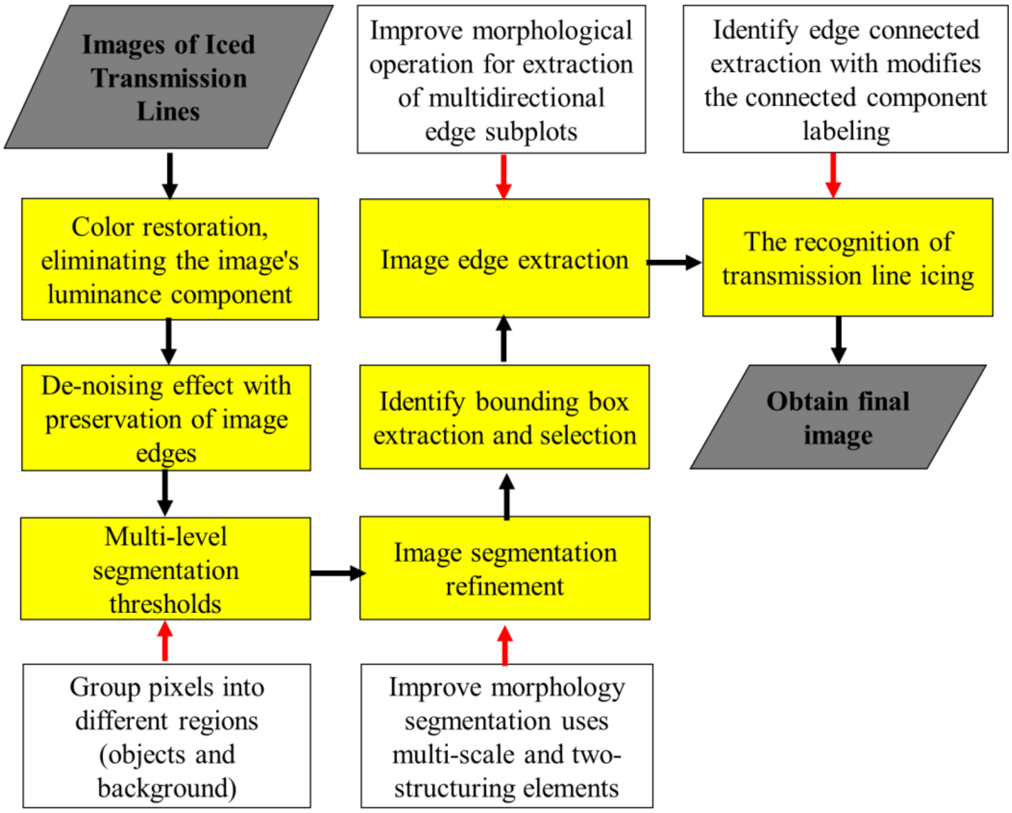

Figure 2. The new scheme for iced transmission line identification and extraction.

Algorithm 1: Image Enhancement Algorithm

Data: I input color image; $\sigma_1,\ \sigma_2,\ \sigma_3$ the scales; $s_1,\ s_2$ the percentage of clipping pixels on each side
Result: Image color restoration
begin
  for each $c\ \in\ \{R,\ G,\ B\}$ do //for each color channel
   for each σ_i do //for each scale
    $O_{ic}(x,y) = \log(I_i(x,y)) - \log(I_i(x,y) * F(x,y))$//convolve the original image
  end
  $O2_c(x,y) = \sum_{n=1}^{N} w_n O_i$ //combining different scales with certain weights
  $O3_c(x,y) = C_i(x,y)O2_i(x,y)$ //color restoration
  $Out_c =$ simplest color balance $(O3_c, s_1,\ s_2)$
end
end

According to Figure 3, the PTLI images for the experiment are prepared for the initial steps, and then all frames are read from the image. The frames are classified into red, green, and blue. The Gaussian surround is calculated after the image frame is read and used as a filter to smooth out the original image. The formula used is as follows:

$$F(x,y) = Ke^{-(x^2+y^2)/(2\times\sigma^2)} \tag{1}$$

The following is an explanation of Equation (1):
$F(x,y)$: Gaussian on pixels (x,y)
e : Exponential;
(x,y) : Pixel coordinates;
σ : Sigma value

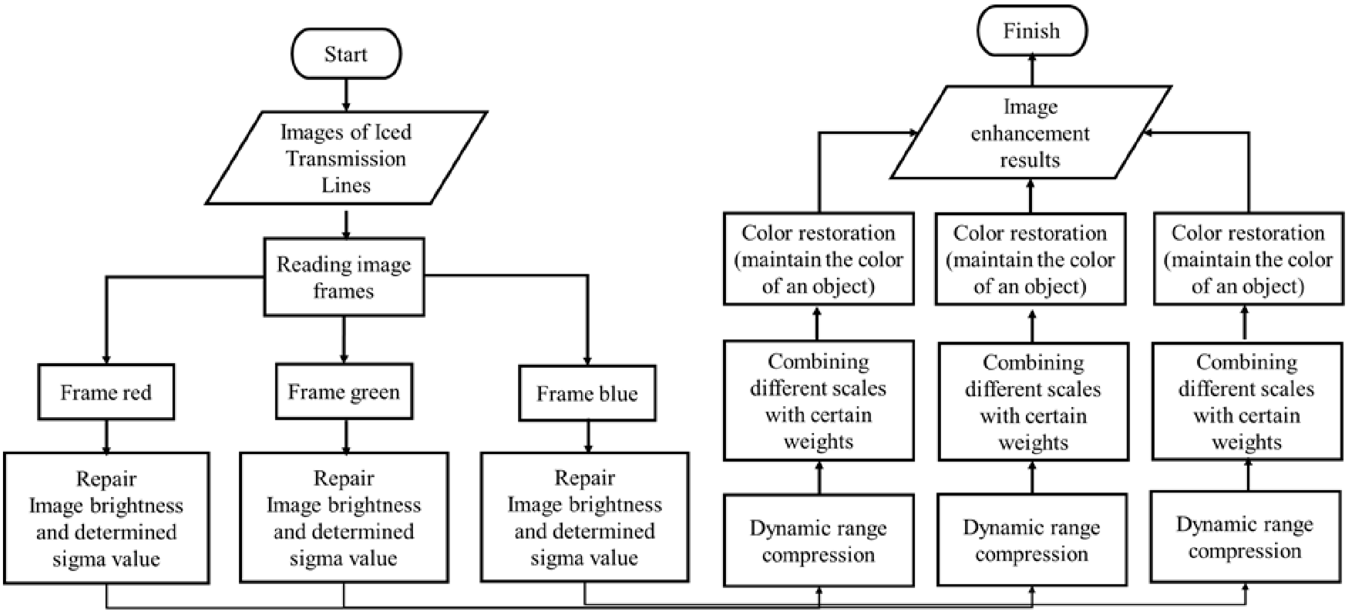

Figure 3. The block diagram for image color restoration.

The first step uses the Gaussian surroundings to increase the image's brightness. This stage is intended for image smoothing beforehand. The Gaussian value is obtained from Equation (1) and determined using three sigma values. The three sigma values used are $\sigma_1 = 15$, $\sigma_2 = 80$, and $\sigma_3 = 250$. However, this value can be changed as needed. Algorithm 1 shows the color restoration algorithm. After the image brightness increases, the next stage is the original image matrix combined with the Gaussian kernel. The image matrix for each color channel was used as the original image matrix. The detail in dark areas is enhanced by a small sigma. At this stage, a member of the class functions center/surround, where the output is defined by the difference between the input value (center) and the average of its environment (surround).

The general mathematical form is as follows:

$$O_i(x,y) = \log(I_i(x,y)) - \log(I_i(x,y) * F(x,y)) \tag{2}$$

where I_i is the input image on the I_{th} color channel, O_i is the output image on the $i-th$ channel, and F is the normalized surround function. This stage is performed on each color channel. The formula used for convolution calculations is as follows:

$$F(x,y) * \; I_i(x,y). \tag{3}$$

The following is an explanation of the convolution formula:
$F(x,y)$: Gaussian on pixels (x,y)
$*$: Convolution
$I_i(x,y)$: Image matrix
i : Color channels (R, G, and B)

Different scales are combined with specific weights at a later stage. The initial stage of this method is to determine the weight to be used. Each weight will be multiplied by the results of each convolution matrix and then added up. Weight values can be adjusted according to the requirements. It affords an acceptable trade-off between a good local dynamic range and a good color rendition. The output is defined as the weighted sum of the outputs of several previous stages (dynamic range compression). The equation for this stage is as follows:

$$O2_i(x,y) = \sum_{n=1}^{N} w_n O_i. \tag{4}$$

where N is the number of scales and w_n is the weight of each scale.

The last step in image enhancement is improving the image quality in relation to the image's brightness by maintaining the color firmness. The concept of color constancy or determination is derived from the human vision system, which attempts to preserve the appearance of an object's color under varying illumination conditions. The chromaticity coordinates are calculated in the first step.

$$I_i'(x,y) = \frac{I_i(x,y)}{\sum_{j=1}^{S} I_j(x,y)}. \quad (5)$$

For the $i-th$ color band, where S is the number of spectral channels, generally $S = 3$ for RGB color space. The restored color is given by:

$$O3_i(x,y) = C_i(x,y)O2_i(x,y). \quad (6)$$

where

$$C_i(x,y) = f\left(I_i'(x,y)\right). \quad (7)$$

For the $i-th$ band of the color restoration function (CRF), the best overall color restoration is defined by:

$$C_i(x,y) = \beta \ \log\left[\alpha I_i'(x,y)\right] \quad (8)$$

For the $i-th$ channel, at position (x,y), the CRF depends on the ratio of the composition of the pixel at (x,y) for that channel value to the total of all of them. Where β is a gain constant and α controls the strength of the normality. A set of β and α values that work for all spectral channels (RGB) is determined by the experiment [27]. β and α are constants, taken at 46 and 125, respectively [27].

3.2. Image De-Noising

Figure 4 shows the block diagram of image de-noising. Based on the block diagram in Figure 4, the input data from this system is the PTLI image that has been restored in color. The color-corrected image still contains noise, so a filter is needed to remove noise and retain critical information in the image. If the image color restoration stage focuses on lighting and color restoration, this stage focuses on filtering out image noise. After the PTLI image data is prepared, the image containing noise will be restored. Then the output from this system is a de-noising image while maintaining the edges of the transmission line. The Gaussian smoothing concept focuses on filter coefficients enhanced in this method by relative pixel intensities. This method obtains the resulting image pixel values from the weighted average of neighboring pixels through a convolution process. The smaller the pixel's spatial weight, the greater the pixel distance to the central pixel analysis in an image, and vice versa. The more significant the difference in intensity between two pixels, the smaller the photometric weight, so the contribution to the weighting is small. Three parameters control this filter method: kernel dimension, standard deviation to control factors of spatial weighting, and standard deviation to control factors of photometric weighting.

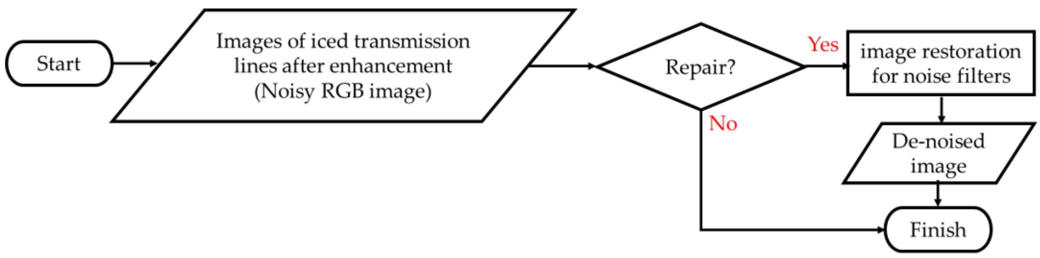

Figure 4. The block diagram of image de-noising.

Spatial weighting in this filter means giving weight to pixels according to the distance between them and those that are the center of analysis in the image. Spatial weight (WS) is the realization of measuring spatial proximity in a Gaussian function that calculates the spatial distance between pixels using Euclidean distance. The calculation of the spatial weight for each pixel is shown in Equation (9).

$$\begin{aligned} W_s[x,u] &= \exp\left\{\frac{-d^2[x],[x,u]}{2\sigma^2 s}\right\}. \\ &= \exp\left\{\frac{-u^2}{2\sigma^2 s}\right\} \end{aligned} \quad (9)$$

With:
$W_s[x,u]$: Spatial weight of each pixel in the kernel;
x : Kernel midpoint (w (0, 0));
u : Neighboring elements in the kernel;
σ_s : Standard deviation for spatial weighting.

Meanwhile, photometric weighting means that the weighting of pixels is based on the difference between the pixel's intensity and the intensity of those that are the center of analysis in the image. Photometric weight (WR) is the realization of measuring the difference in intensity based on the photometric similarity in the Gaussian function, which measures the difference in intensity between pixels using the Euclidean distance. The calculation of the photometric weight at each pixel is shown in the following equation:

$$\begin{aligned} W_s[x,u] &= \exp\left\{\frac{-d^2\{g[x],g[x-u]\}}{2\sigma^2 R}\right\} \\ &= \exp\left\{\frac{-\{g[x],g[x-u]\}^2}{2\sigma^2 R}\right\}. \end{aligned} \quad (10)$$

With:
$W_s[x,u]$: Photometric weight per pixel in the kernel;
x : Kernel midpoint (w(0, 0));
u : Neighboring elements in the kernel;
$g[x]$: Pixels, which are the center of analysis in degraded images;
$g[x-u]$: Neighboring pixels of pixel g $[x]$;
σ_R : Standard deviation for photometric weighting.

The two weights (spatial and photometric) are normalized to one weight value (W) as in Equation (11).

$$W[x,u] = W_s[x,u] * W_R[x,u]. \quad (11)$$

After weighting the pixels, the resulting pixel values can be found in Equation (12).

$$f[x] = \frac{\sum_{u=-N}^{N} W[x,u] g[x-u]}{\sum_{u=-N}^{N} W[x,u]}. \quad (12)$$

With:
$W[x,u]$: Neighboring weight values in the W weight matrix;
$f[x]$: Calculated pixel value.

3.3. Multi-Level Threshold

This subsection explains a multi-level segmentation threshold that marks out the targets of interest in an image. The goal at this stage is to separate the transmission line icing pixels from the background. The selection of thresholds is critical and related to the good or bad results after segmentation. With proper segmentation, an image can be described simply by utilizing meaningful things, which are easier to analyze. A multi-level segmentation threshold is a process that splits the degree of gray in an image into transparent regions based on several points or threshold values. A multi-level threshold separates pixels into classes or groups. Pixels in the same class will have a degree of grayscale within a specific range obtained from several thresholds. Figure 5 shows a block diagram of the multi-level threshold segmentation process.

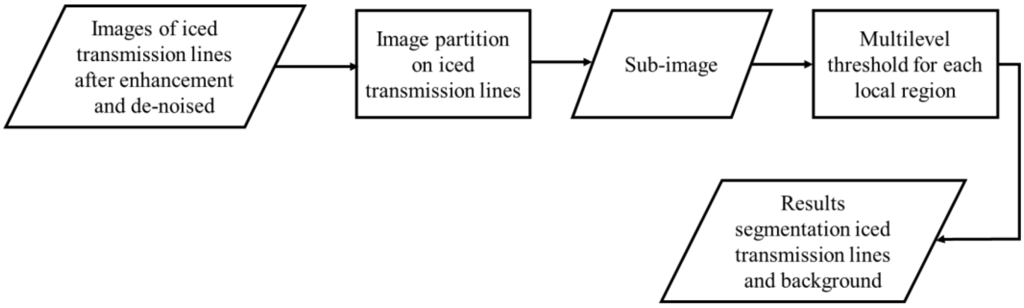

Figure 5. The block diagram of the multi-level threshold segmentation process.

Initially, the input image is divided into several sub-images. In the next stage, a multi-level threshold is applied based on the histogram information of each sub-image. Two local threshold values divide the image into two regions: the transmission line icing and the background. The local threshold value is the threshold value for each sub-image. The process is repeated until all sub-images are segmented. Figure 6 shows in detail the multi-level threshold process.

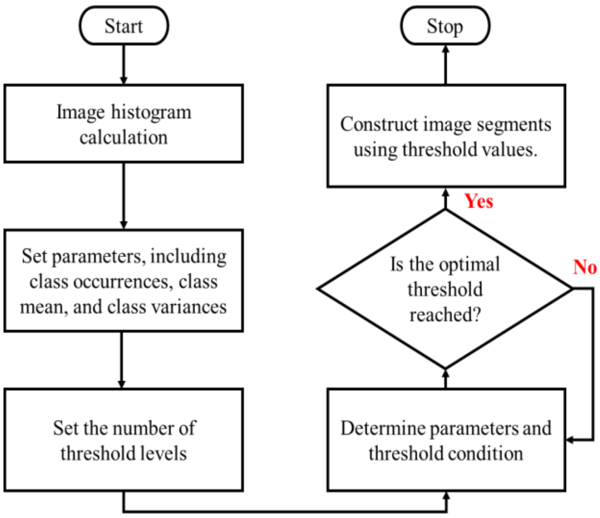

Figure 6. The block diagram of the multi-level threshold for each local region.

$$p_i = \frac{n_i}{N}, \qquad p_i \geq 0, \; \sum_{i=1}^{L} p_i = 1. \tag{13}$$

The pixels of the image are separated into a good number of k levels of preferred thresholds. The image is sectioned into $k+1$ levels or classes, which are denoted by $C_o = \{0, 1, \ldots, t_1\}, \ldots, C_n = \{t_n + 1, t_n + 2, \ldots, t_{n+1}\}$, and $C_k = \{t_k + 1, t_k + 2, \ldots, L-1\}$. Consequently, the class occurrences W_n, the mean class levels (μ_n), and the class variances (σ_n^2), respectively, are computed as in Equations (14)–(16).

$$W_n = \sum_{i=t_n+1}^{t_n+1} p_i. \tag{14}$$

$$W_n = \frac{\sum_{i=t_n+1}^{t_n+1} i p_i}{W_n}. \tag{15}$$

$$\sigma_n^2 = \frac{\sum_{i=t_n+1}^{t_n+1} \; p_i(i-\mu_n)^2}{W_n}. \tag{16}$$

The within-class variances σ_{wc}^2 of all segmented classes of pixels are given in Equation (17).

$$\sigma_{wc}^2 = \sum_{n=0}^{k} W_n \, \sigma_n^2. \tag{17}$$

The between-class variances measure the spare ability among all classes, as in Equation (18).

$$\sigma_{bc}^2(k_1, k_2, \ldots, \; k_L) = \sum_{n=0}^{k} W_n(\mu_n - \mu_T)^2. \tag{18}$$

The process is repeated until all sub-images are segmented. Figure 6 shows in detail the multi-level threshold process.

3.4. Mathematical Morphology

There are many kinds of operators in mathematical morphology, among which the most basic ones are dilatation and erosion. The opening and closing operations are two critical secondary operations based on the dilatation and erosion operations. The morphological calculation process from a mathematical perspective is as follows:

It assumes that Ω represents two-dimensional Euclidean space. B is a mathematical structural element that operates with A, where A and B are subsets of Ω. Φ represents empty sets. The erosion operation (sometimes called "Minkowsky subtraction") is defined as follows:

$$A \; \Theta \; B = \{\mathrm{x} | [(B)x] \; A\}. \tag{19}$$

Based on Equation (19), the erosion of A by B means that B contains the set of all points x in A after B translates x. Corrosion is an operation that shrinks or refines A . The dilation operation (sometimes called "Minkowsky addition") is defined as follows:

$$A \oplus B = \left\{\mathrm{x} \middle| \left[\left(\overline{B}\right)x \right] \; \cap A \right\} \neq \Phi. \tag{20}$$

Which represents the expansion of B to A. The operator $\overline{B}$ is the structural element of B's origin image. The expansion of B to A refers to the set of all displacements x based on the translation of the image structure element x. Dilation refers to growing or coarsening pixels in a binary image. Opening and closing are critical morphological filters for image smoothing, which is good for smoothing light and dark image features. These smoothed features could be extracted for image analysis. However, based on the characteristics of the transmission line icing image used in this research, it only uses a closing operator to maintain its edge contour. The closing operation for the filter is described as follows:

$$A \; \circ B = (A \; \Theta \; B) \oplus B. \tag{21}$$

where the element B first dilates A, and then B erodes the result.

When the morphology is applied in the image processing, A is to process the image, and B is a structural element. The gaps and holes are connected to the neighboring objects and smooth objects. In addition, both operations will not significantly change the image area or shape. The binary image obtained after the segmentation threshold contains a transmission line covered with iced targets, a background, and other interference objects. In addition, the segmentation result of the transmission line is still rough, so it is necessary to enhance the object. Mathematical morphology is a nonlinear filtering method that can be applied to simplify image data while maintaining its essential shape characteristics. In most cases, a single structural element realizes the mathematical morphology, which makes edge detection of transmission line effects poor. A single structural element can only detect edge structural element information in the same direction, while the other directions are not edge-sensitive.

Morphological operations are applied to segmented images to smooth the image. The mathematical morphology has been enhanced in this study. Figure 7 shows a flowchart for image segmentation refinement using mathematical morphology.

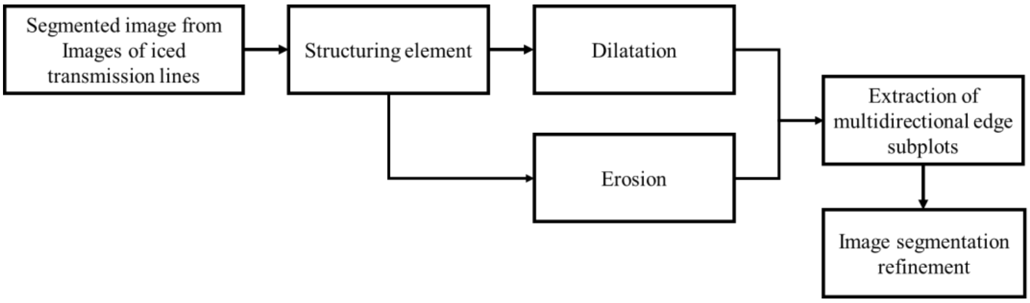

Figure 7. The flowchart for image segmentation refinement using mathematical morphology.

The scheme extended a compromise method, which uses multiscale and two structuring elements for alternating sequences of morphological opening and closing filtering to smooth the image and remove the noise. It effectively solves the problems posed by single structural elements. Equation (22) contains a morphological edge detection operator with multiscale elements and two structuring elements, where $F(x, y)$ is the gray image and $B(s, t)$ is the structuring element:

$$E(F) = (F \circ B) \oplus A - (F \bullet B) \Theta A. \tag{22}$$

where A and B, respectively, are diamond-type 5×5 structuring elements and cross-shaped 3×3 structuring elements.

$$A = \begin{bmatrix} 0 & 0 & 1 & 0 & 0 \\ 0 & 1 & 1 & 1 & 0 \\ 1 & 1 & 1 & 1 & 1 \\ 0 & 1 & 1 & 1 & 0 \\ 0 & 0 & 1 & 0 & 0 \end{bmatrix} \quad B = \begin{bmatrix} 0 & 1 & 0 \\ 1 & 1 & 1 \\ 0 & 1 & 0 \end{bmatrix}. \tag{23}$$

A and B are structural elements with different scales. Although the ability to eliminate noise is weak, small-scale structural elements B can better retain image edge information. Large-scale structural elements A can remove image noise well, but they miss some transmission line edge information. So, multiscale structure elements and two structures can effectively remove image noise and retain good segmentation of the iced line result information. This improved mathematical morphology removes small dark spots and connects small bright cracks. Otherwise, it is used to close the dark gaps between light features.

3.5. Bounding Box Identification

Bounding box identification can separate specific areas of the PTLI image that are considered more important than other objects. In the PTLI image with ROI coding, that area will have higher image quality than the background.

The method for determining the bounding box is: if the iced transmission line forecast image is $r(x, y)$, then $r_i(x, y)$ are the connected components (regions) contained in $r(x, y)$, with $i = 1, 2, \ldots, n$; n is the number of regions; or $r_i(x, y) \in r(x, y)$. A bounding box is obtained for each $r_i(x, y)$ based on the iced line forecast image. A bounding box is an imagined box that encloses a specified area that surrounds $r_i(x, y)$. The bounding box for each $r_i(x, y)$ is determined based on the spatial coordinates of the upper-left (UL), upper-right (UR), lower-left (LL), and lower-right (LR) pixels. Suppose the size of the image $r_i(x, y)$ is $M \times N$, where M is the number of pixel rows and N is the number of pixel columns. The illustration of the bounding box $r_i(x, y)$ is shown in Figure 8. The flow for determining the bounding box for each region $r_i(x, y)$ is shown in Figure 9. Yellow boxes indicate connected component bounding boxes (regions). The bounding box obtained only surrounds the transmission line icing area (Figure 10a). The bounding box's size is adjusted again by widening it to cover the entire area of the line icing. Each bounding box spatial coordinate (UL, UR, LL, and LR) is widened by adding k pixels (Figure 10b). The k value is obtained from the average iced transmission line pixel width.

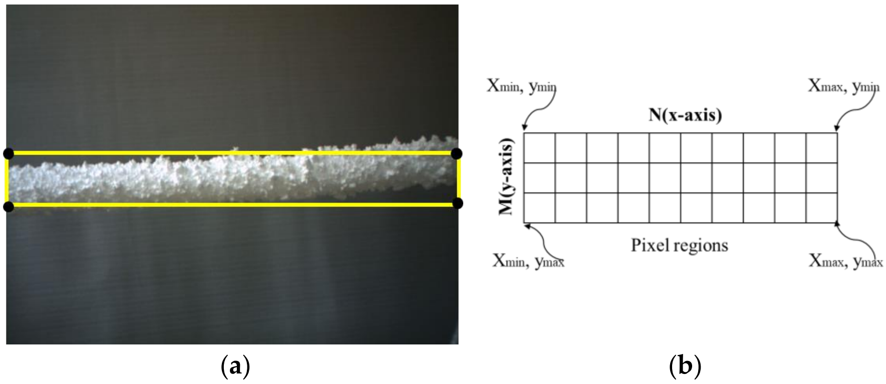

Figure 8. An illustration of bounding box identification. (**a**) RGB image; (**b**) An image described in pixels.

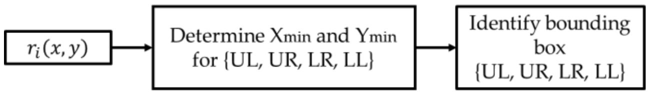

Figure 9. The flow of bounding box determination.

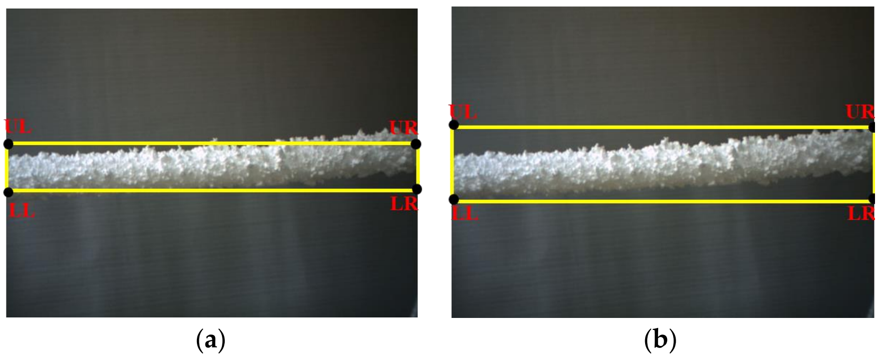

Figure 10. The bounding box (**a**) before widening and (**b**) after extension with k pixels in size.

3.6. Image Edge Extraction

The results of line icing segmentation were obtained in the previous stage by selecting the region of interest. After the segmentation process, the edge detection results are still unclear, so improving the mathematical morphology used to emphasize the object's shape (transmission line icing) is necessary. At this stage, the PTLI image edge extraction will be explained. Mathematical morphology is also used for the edge extraction of iced lines. In this method, the focus is on enlarging bright regions and shrinking dark regions. Figure 11 shows the block diagram for edge extraction using improved mathematical morphology.

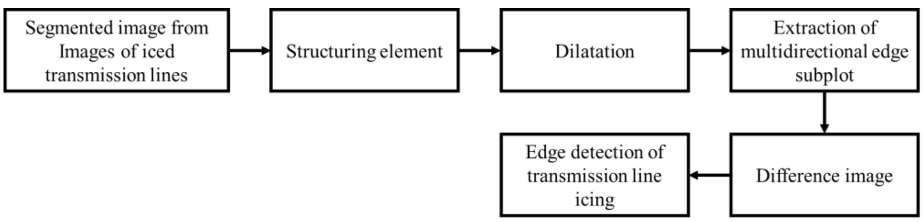

Figure 11. The block diagram for edge extraction using improved mathematical morphology.

These morphological operations are performed on images based on shapes using structuring elements. It is a matrix containing '1' and '0', where '1' are called neighborhood pixels. The output pixel is determined by using these processing pixel neighbors. Here, the structuring element is used to dilate the image for edge extraction. The dilation operations are performed on images with different structuring elements by adding a pixel at an object boundary based on the structuring elements. The rule for finding output pixels is the maximum input pixels in the neighborhood matrix.

3.7. Line Icing Identification

The next step is the identification of the line of the PTLI. At this stage, the upper and lower lines of the iced transmission line are determined for further analysis based on 3D measurements. This study uses a connected component labeling modification to distinguish between the upper and lower lines. This method gives a unique label to each object in an image by converting a binary image into a symbolic image, in which all pixels belonging to each connected component are uniquely labeled. So, the PTLI lines can be distinguished using unique labels (the top and bottom lines). In computer vision, connected component labeling detects connected regions in binary digital images.

The first scan assigns provisional labels to object pixels and records equivalences. Label equivalences are resolved during or after the initial scan. Then, all equivalent labels on the second scan are replaced by representative labels. These two-scan labeling algorithms have some defects since a recursive algorithm may possibly cause overflow. In addition, this method produced a good performance but took a long time. The implementation of image processing systems requires faster computer processing. Based on the above problems, this study modified the classic method for labeling connected components. This research uses a one-time scanning algorithm with a scanning mask of size three so that the labeled pixels adjacent to the current object pixels will have the same label using the last-in-first-out stack processing scheme. The classic algorithm is enhanced by employing a larger scanning mask pattern to reduce the processing time and memory space required for analyzing neighboring pixels. The concept of scanning mask technology to find 4-connectivity is presented in this subsection. The approach is that the image with the raster scanning direction is scanned from top to bottom, left to right, and pixel by pixel. The fundamental operation of each iteration is shown in Figure 12. In this method, the pixels will be mask scanned until an unlabeled object X pixel is found in the input image. Then, the object pixel X is labeled with the same label number as one of its neighboring pixels, P, Q, R, or S. In the case of label conflicts, equality can be resolved by choosing the lower number, i.e., $label(X) = \min(Label(P),\ label\ (Q),\ label\ (R),\ label(S))$.

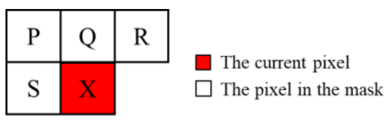

Figure 12. The scan mask with 4-connectivity (the current pixel X is compared to its neighbor's pixels P, Q, R, and S).

Figure 13 illustrates an example of the labeling used in this study. The labeling procedure utilized in this study is described below. The red arrows in Figure 13 indicate the labeling process, while the black arrows block indicates the process of labeling area expanded.

1. Unlabeled object pixels with coordinates (0, 0) are shown in the scan mask, represented by dotted lines.
2. Based on point (b) in Figure 13, the label with '1' in the current pixel is processed.
3. The mask is scanned at the next unlabeled pixel (2, 0).
4. At point (d), the labeling of pixels with '2' is illustrated. Currently, there are two labels on the pixel objects.
5. The mask is scanned at the next unlabeled pixel (3, 0).

6. Process of labeling with '2' again because its neighboring pixels are already labeled '2', so that expanded the labeling area.
7. The mask is scanned at the next unlabeled pixel (1, 1) in point (g).
8. Pixels are labeled with '1' because the diagonals of adjacent pixels (0, 0) are already labeled with '1'.
9. Because the pixels at location (1, 1) are labeled with '1', the labeling area expanded.
10. The labeled areas '1' and '2' intersect, so the labeled area is expanded to a square of four pixels containing (0, 0), (0, 1), (1, 0), and (1, 1) using the expansion rule.
11. The mask is scanned at the next unlabeled pixel (2, 1).

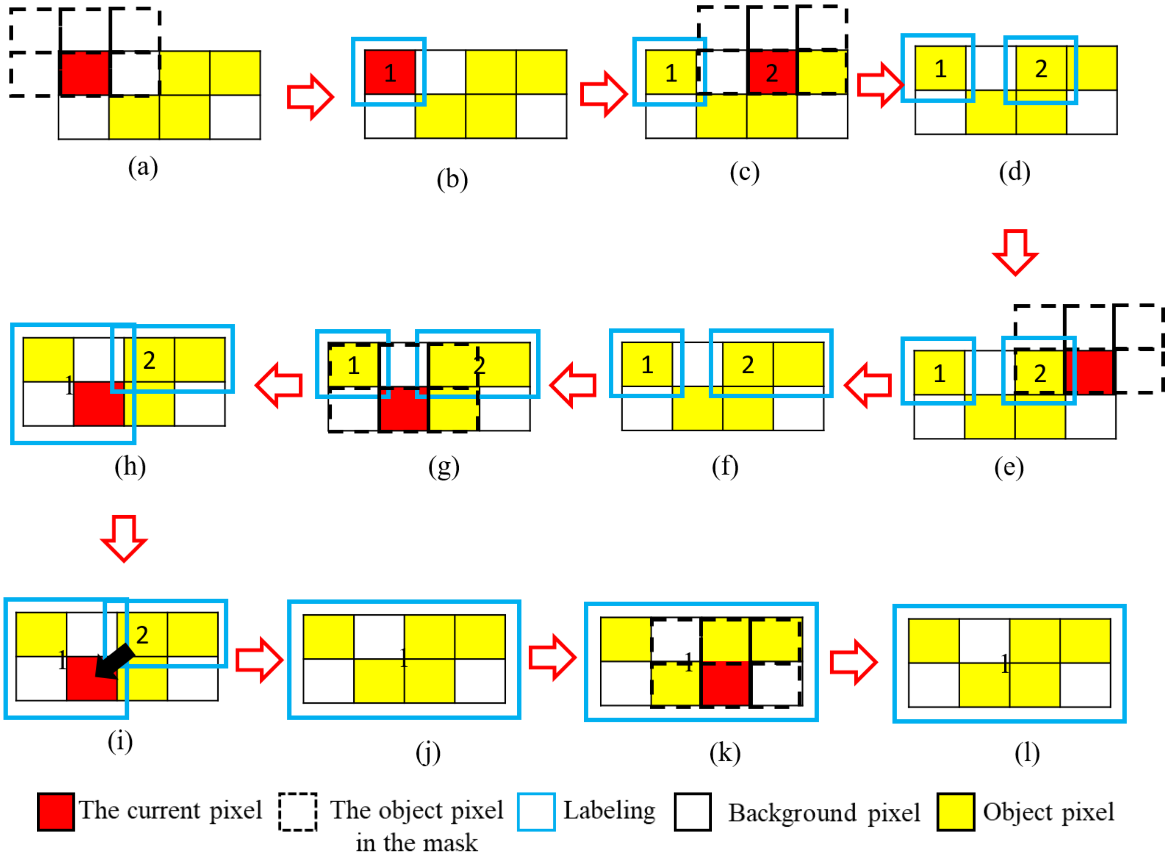

Figure 13. An example of the labeling used in this research. (**a**) Unlabeled object; (**b**) The process of labeling '1' on the current pixel; (**c**) the mask is scanned at the next unlabeled pixel (2, 0); (**d**) The process of labeling '2'; (**e**) the mask is scanned at the next unlabeled pixel (3, 0); (**f**) The process of labeling '2' and expanded the labeling area; (**g**) The mask is scanned at the next unlabeled pixel (1, 1); (**h**) Pixels are labeled with '1' because the diagonals of adjacent pixels (0, 0) are already labeled with '1'; (**i**) The process of labeling area expanded; (**j**) The labeled areas '1' and '2' intersect; (**k**) The mask is scanned at the next unlabeled pixel (2, 1); (**l**) The eight connected neighboring pixels have their labels updated.

Labeled '1' because the left pixel has been labeled "1". Here, all eight connected neighboring pixels update their labels with minimum values.

4. Ice Thickness Calculation Using 3D Measurement

The principal indicator of an ice disaster is ice thickness. This section describes a method for ice thickness measurement based on our proposed iced transmission line identification scheme. After obtaining the key point through the point-matching algorithm to find similar key points, the key point is used as a reference point in determining 3D coordinates. Figure 14 illustrates the flowchart of the ice thickness calculation.

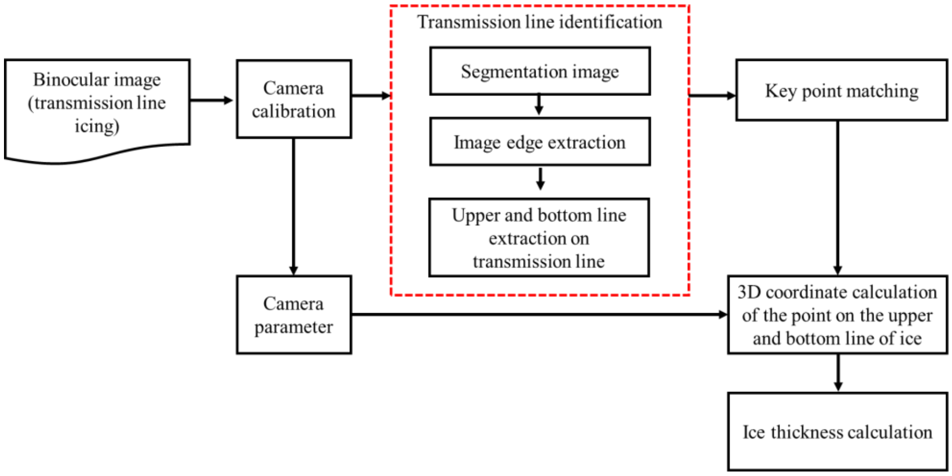

Figure 14. The flowchart of the ice thickness calculation.

This process begins with determining the intrinsic and extrinsic camera parameters through calibration. This initialization aims to investigate the relationship between 3D world coordinates and 2D image coordinates, which will later be utilized as a reference for determining the 3D point at each key point. This paper uses Zhang Zhengyou's calibration methods [28]. The calibration process provides the internal parameters of the camera, such as focal length and distortion factor, as well as the external parameters, including the rotation matrix and translation matrix. The calibration process is shown in Figure 15. Multiple sets of calibration images can be captured by adjusting the relative positions of the camera and the plane target. The method assumes an ideal pinhole camera model and quickly solves the mapping matrix between the target and image planes using the equations established by the calibration images. The internal and external camera parameters are then obtained by matrix decomposition. Finally, all the obtained linear parameters and the simultaneous addition of lens distortion parameters undergo optimization searches to obtain the optimal solution for all parameters.

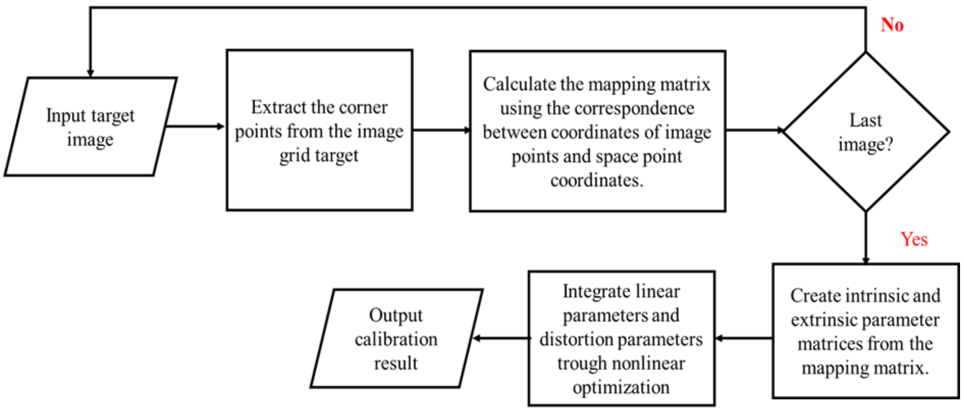

Figure 15. The flowchart of Zhang Zhengyou's camera calibration method.

After setting up the camera parameters, the next step is linear triangulation. Binocular stereo vision relies on the disparity value of the same point in different viewing angle images to calculate the depth value using the triangulation principle, i.e., the projection points p_1 and p_2 of a specific point P on the left and right image pairs in space. The camera structure parameters are used to calculate the 3D space coordinates of point P.

As shown in Figure 16, it is assumed that the left camera coordinate system $O - xyz$ is located at the origin of the world coordinate without rotation, the image coordinate system is $O_l - x_l y_l$, and the effective focal length is f_l. The right camera coordinate system is $O_r - x_r y_r z_r$, and the image coordinate system is $O_r - x_r y_r$. The effective focal length is

f_r, and the relationship between the left and right camera coordinate systems and their corresponding image coordinate systems can be obtained from the camera perspective transformation model:

$$\begin{bmatrix} x_l \\ y_l \\ 1 \end{bmatrix} = \frac{1}{s_l} \begin{bmatrix} f_l & 0 & 0 \\ 0 & f_l & 0 \\ 0 & 0 & 1 \end{bmatrix} \begin{bmatrix} x \\ y \\ z \end{bmatrix}. \tag{24}$$

$$\begin{bmatrix} x_r \\ y_r \\ 1 \end{bmatrix} = \frac{1}{s_r} \begin{bmatrix} f_r & 0 & 0 \\ 0 & f_r & 0 \\ 0 & 0 & 1 \end{bmatrix} \begin{bmatrix} x_r \\ y_r \\ z_r \end{bmatrix} \tag{25}$$

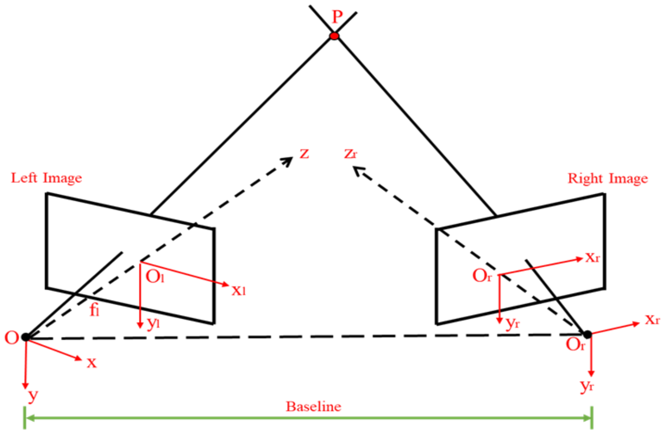

Figure 16. The 3D measurement model for binocular stereo vision in space.

Among them, s_l and s_r are scale factors that satisfy $\frac{s_l}{z} = 1$ and $\frac{s_r}{z} = 1$, respectively. (x_l, y_l) and (x_r, y_r), respectively, represent the image coordinate system of the projection points p_1 and p_2 of point P on the left and right images. (x, y, z) and (x_r, y_r, z_r) represent the left and right camera coordinate systems, respectively. The left and right camera coordinate systems $O - xyz$ and $O_r - x_r y_r z_r$ can establish the positional relationship by expressing the conversion relationship of the binocular structure. The space conversion matrix can express M_{lr} as follows:

$$\begin{bmatrix} x_r \\ y_r \\ z_r \end{bmatrix} = M_{lr} \begin{bmatrix} x \\ y \\ z \\ 1 \end{bmatrix} \begin{bmatrix} R_{11} & R_{12} & R_{13} & T_x \\ R_{21} & R_{22} & R_{23} & T_y \\ R_{31} & R_{32} & R_{33} & T_z \end{bmatrix} \begin{bmatrix} x \\ y \\ z \\ 1 \end{bmatrix}. \tag{26}$$

Among them is the space transformation matrix $M_{lr} \begin{bmatrix} R & T \end{bmatrix}$, where R and T are the rotation and translation matrices between the $O - xyz$ coordinate system and the $O_r - x_r y_r z_r$ coordinate system, respectively. According to Formulas (25) and (26), for the spatial point in the $O - xyz$ coordinate system, the corresponding relationship between the image plane points of the left and right cameras can be transformed into:

$$\begin{bmatrix} x_r \\ y_r \\ 1 \end{bmatrix} = \frac{1}{s_r} \begin{bmatrix} f_r R_{11} & f_r R_{12} & f_r R_{13} & f_r T_x \\ f_r R_{21} & f_r R_{22} & f_r R_{23} & f_r T_y \\ R_{31} & R_{32} & R_{33} & T_z \end{bmatrix} \begin{bmatrix} zX_l / f_l \\ zY_l / f_l \\ z \\ 1 \end{bmatrix}. \tag{27}$$

Therefore, according to Formulas (24) and (27), the 3D coordinates of the spatial point can be obtained:

$$\begin{cases} x = \frac{zX_l}{f_l} \\ y = \frac{zY_l}{f_l} \\ z = \frac{f_l(f_rT_x - x_rT_z)}{x_r(R_{31}X_l + R_{32}Y_l + f_lR_{33}) - f_r(R_{11}X_l + R_{12}Y_l + f_lR_{13})} \\ = \frac{f_l(f_rT_y - Y_rT_z)}{Y_r(R_{31}X_l + R_{32}Y_l + f_lR_{33}) - f_r(R_{21}X_l + R_{22}Y_l + f_lR_{23})} \end{cases}. \tag{28}$$

In summary, the internal parameters' focal length f_l and f_r of the two cameras, the external parameters rotation matrix R and translation matrix T, and the image coordinates (x_l, y_l) and (x_r, y_r) of the feature point P in the left and right cameras are known. In the case of 3D space, the coordinates of P can be obtained. As we all know, the internal and external parameters of the camera can be obtained through camera calibration. Therefore, only the coordinates of the image coordinate system of the point P in the left and right cameras, that is, the corresponding relationship between the points in the left and right images, can be used to obtain the 3D space coordinates of P. Subsequently, iced transmission line identification is used to find the top and bottom boundaries of ice formed on power transmission lines. Next, the iced transmission line's 3D coordinates for the key points are computed using the key point matching method. Finally, the ice thickness is calculated.

The ice thickness is estimated after the 3D coordinate points (x, y, x) are obtained. The 3D coordinate graphed in the $xyz - space$ is more difficult than in the $xy - plane$ because depth perception is required. One can use projections onto the coordinate planes to simplify plotting points. The projection of a point (x, y, x) onto $xy - plane$ is obtained by connecting the point to the $xy - plane$ by a line segment perpendicular to the plane and calculating the intersection of the line segment with the plane. In this investigation, ice thickness was calculated using a three-dimensional Euclidean distance. Figure 17 shows a schematic diagram of 3D Euclidean distances.

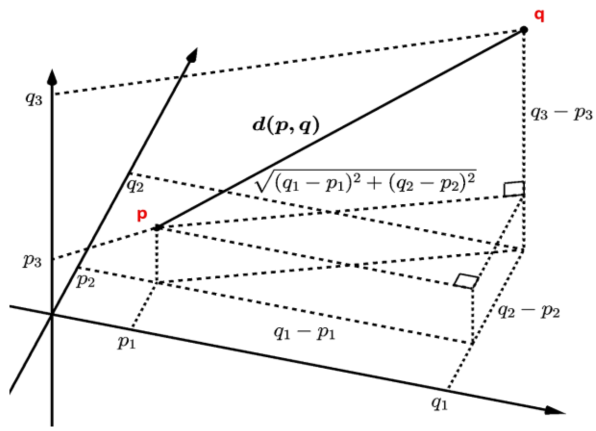

Figure 17. The diagram of 3D Euclidean distance.

According to Figure 17, it will be calculated from the distance $P = (x_1,\ y_1, z_1)$ to $q = (x_2,\ y_2, z_2)$ in $xyz - space$. Then, the calculation formula is shown as follows:

$$d(P, q) = \sqrt{(x_2 - x_1)^2 + (y_2 - y_1)^2 + (z_2 - z_1)^2} \tag{29}$$

For example, the distance between $P = (2,\ 3,\ 1)$ and $q = (8, -5,\ 0)$ is:

$$d(P, q) = \sqrt{(8 - 2)^2 + (-5 - 3)^2 + (0 - 1)^2}$$

$$d(P, q) = \sqrt{36 + 64 + 1}$$

$$d(P, q) = \sqrt{101}$$

$$d(P, q) \approx 10.05$$

The three-dimensional calculation for ice thickness is adopted from Formula (29) above. Calculate the distance between the edge of the top line and the edge of the bottom line using Formula (30). After knowing the distance between both sides of the iced line, subtract the distances from the diameter of the lines without icing (60 mm) so that the ice thickness can be found. The formula for measuring ice thickness can be seen below.

$$Ice\ thickness = D_{tb} - d_l. \tag{30}$$

where D_{tb} is the distance between the top and bottom edge lines and d_l is the diameter of the cable without an ice load. Therefore, the ice thickness calculation in this research can be applied to measure line icing in straight or curved positions. Figure 18 shows an illustration of the ice thickness calculation using 3D measurements. According to Figure 18, the gold line shows the line detection results at the top, while the light blue line shows the line detection results at the bottom. The star element labeled A is a key point that will be used for ice thickness measurement in that area, while the other stars indicate key points in the PTLI scene. Based on Figure 18, to calculate the ice thickness in area A on the iced line, first find the farthest points of the iced line in the upper and lower boundary areas from point A to find points p and q. Point p is the farthest point from the upper line, and point q is the farthest from the lower line. If we have points p and q, we can easily find the ice thickness using Formulas (29) and (30).

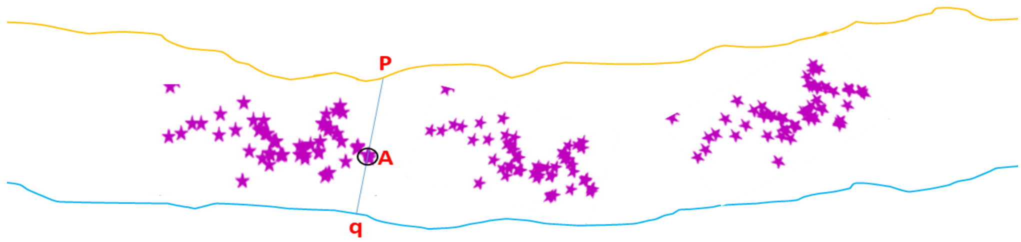

Figure 18. An illustration of the ice thickness calculation using 3D measurements.

5. Experiment and Evaluation

On the PTLI dataset, we verified the effectiveness of our proposed method on the ice thickness measurement. Additionally, on the PTLI scene dataset, the overall performance of our approach was evaluated using the confusion matrix. The segmentation results from the proposed method are compared with ground truth images. The proposed method aims to classify transmission line icing pixels on ROI as true positive, false negative, or false positive, as represented by accuracy, precision, and recall.

5.1. Dataset and Evaluation Matrix

5.1.1. Dataset

Our proposed method's iced transmission line identification performance is evaluated on the collected simulated PTLI scene dataset. A series of simulated PTLI scenes were independently generated to facilitate the collection of icing image data. Long cylindrical pearl cotton (Expandable Polyethylene, EPE) is used to simulate the transmission line; polystyrene foam (Expanded Polystyrene, EPS) is attached to its surface as a simulated ice coating; and pearl cotton is used to simulate the background of the iced transmission line. So far, the iced transmission line scene is built and shown in Figure 19. The image pairs of the simulated PTLI dataset are collected using a Daheng binocular camera. It is huge and challenging work to do pixel-level labeling on collected images. Thus, the proposed method's measurement results of ice thickness are directly compared with the manual measurement results.

Figure 19. A simulated ice scene image.

5.1.2. Evaluation Matrix

The segmentation results from our proposed scheme are compared with ground truth images, which are segmented manually. The proposed scheme aims to classify transmission line icing pixels on ROI as true positive, false negative, or false positive, as represented by accuracy, precision, and recall. The system testing process is conducted using the confusion matrix. The confusion matrix can be interpreted as a tool that analyzes whether the classifier is good at recognizing tuples from different classes. The values of True Positive (TP) and True-Negative (TN) provide information when the classifier in classifying data is true, while False Positive (FP) and False-Negative (FN) provide information when the classifier is incorrect in classifying data. Table 2 is the confusion matrix used to determine TP, TN, FP, and FN. After obtaining the TP, TN, FP, and FN values, accuracy, precision, recall, and specificity can be calculated using Equations (31)–(34).

Table 2. Confusion matrix.

		Ground Truth	
		Transmission Line	Not Transmission Line
Our Scheme	Transmission line	True Positive (TP)	True Negative (TN)
	Not transmission line	False Positive (FP)	False Negative (FN)

Accuracy describes how often the model is classifying correctly. The accuracy can be calculated using Equation (31).

$$Accuracy = \frac{TP + TN}{TP + TN + FP + FN}. \tag{31}$$

Precision describes the accuracy between the requested data and the predicted results provided by the model. To calculate precision, use Equation (32).

$$Precision = \frac{TP}{TP + FP}. \tag{32}$$

Recall, or sensitivity, describes the success of the model in retrieving information. Equation (33) can be utilized to compute recall.

$$Recall = \frac{TP}{TP + FN} \tag{33}$$

Specificity is used to measure the percentage of correctly identified negative data. To calculate specificity, use Equation (34).

$$Specificity = \frac{TN}{TN + FN}. \tag{34}$$

5.2. Performance of the Proposed Method

This section presents each stage of the experiment and evaluation results in our proposed scheme for identifying and extracting iced transmission lines. Three images with different illumination conditions and backgrounds are presented in this section as samples to test our proposed scheme. The three images are shown in Figure 20.

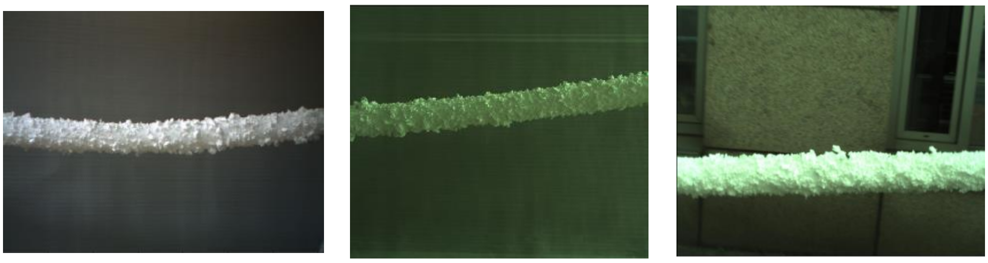

(**a**) (**b**) (**c**)

Figure 20. The original image with different illumination conditions and backgrounds. (**a**) Image 1; (**b**) Image 2; (**c**) Image 3.

5.2.1. Image Color Restoration

At this stage, the image that appears dim and hazy with a hue distorted from the original color is corrected by preserving the original color. In general, this stage is used for color restoration; the lighting component in the image is removed. Figure 21 shows the image after color restoration using the method in this paper. Figure 21 shows that our method can restore image color while preserving the original color. The iced transmission line is brighter and more precise than the original image.

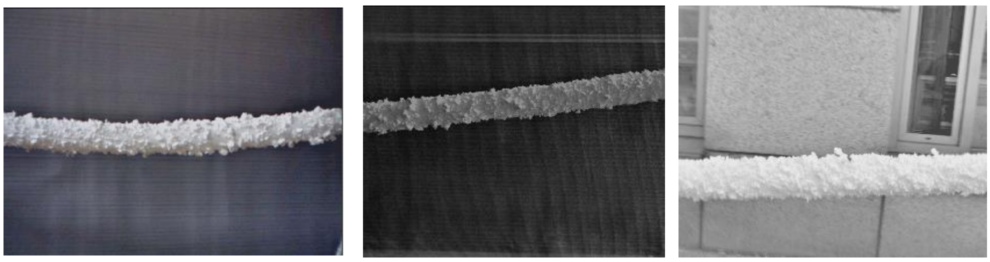

(**a**) (**b**) (**c**)

Figure 21. The result of image color restoration. (**a**) Image 1; (**b**) Image 2; (**c**) Image 3.

5.2.2. Image De-Noising

In this stage, unwanted noise is removed and valuable information is preserved, such as transmission line edges and transmission line icing textures. Figure 22 shows the image after the de-noising effect (filter noise). The proposed method in this paper for image de-noising has been successfully applied. Based on Figure 22, the image after de-noising is smoother and has less noise, and the edges and texture of the transmission line icing are maintained.

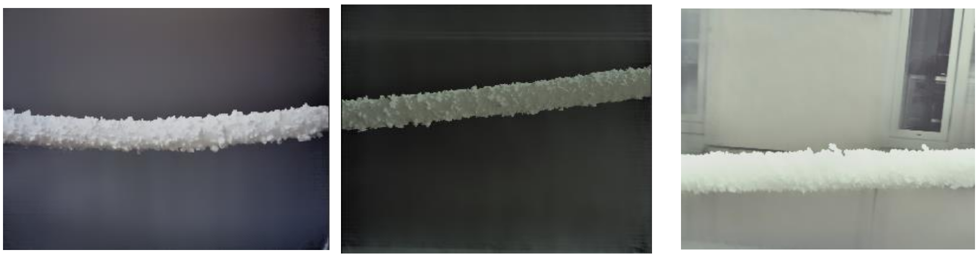

(a) (b) (c)

Figure 22. The image after the de-noising effect. (**a**) Image 1; (**b**) Image 2; (**c**) Image 3.

5.2.3. Multi-Level Threshold Segmentation

At this stage, the process separates the iced transmission line from a complex background containing objects and other noise. Pixels are generally grouped into various regions (objects and backgrounds) in this method. Figure 23 shows the results of the multi-threshold segmentation.

(a) (b) (c)

Figure 23. The results of the multi-threshold segmentation. (**a**) Image 1; (**b**) Image 2; (**c**) Image 3.

Figure 23 shows that our method successfully clusters pixels into different regions (object and background). After dividing several regions in the multi-threshold stage, the image successfully recognizes transmission line icing objects. At the same time, the background at this stage is eliminated.

5.2.4. Mathematical Morphology

Morphological operations are applied to segmented images to refine them. The gaps and holes are connected to neighboring objects and smooth objects. Figure 24 shows the result after the mathematical morphology operation.

(a) (b) (c)

Figure 24. The result after mathematical morphology. (**a**) Image 1; (**b**) Image 2; (**c**) Image 3.

Based on Figure 24, morphological operations were successfully applied to segmented images. The image after the morphology operation is better because gaps and holes are connected to neighboring and smooth objects. The morphology operation will not change the image area or shape significantly.

5.2.5. Identifying the Bounding Box

This stage consists of four parts. First, the image resulting from multi-threshold segmentation and morphology is changed again to an RGB image, selecting only the transmission line icing object and removing the background and foreground. Then, the image is identified in the $X - min$ and $Y - min$ parts of the object to determine the upper left and right, then the lower left and right. Finally, the RGB image is selected on the ROI and returned to the binary image for further processing. Table 3 shows the process of selecting the region of interest.

Table 3. The process of selecting the region of interest.

No	Binary Image (after Multi-Threshold)	RGB Image (the Result of Multi-Threshold)	ROI Image
1			
2		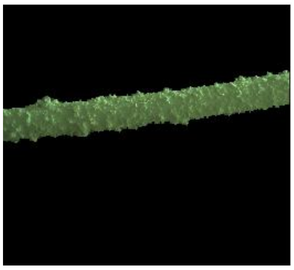	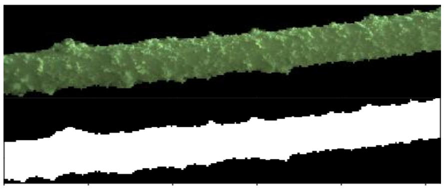
3		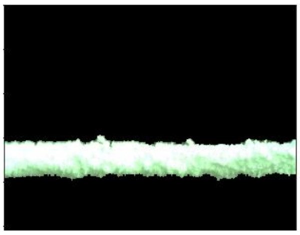	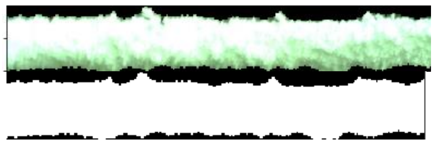

5.2.6. Image Edge Extraction

The iced transmission line segmentation results were obtained by selecting the region of interest in the previous stage. Mathematical morphology is improved to expand the white area, emphasize the object's shape (transmission line icing), or determine the perimeter of objects within a binary image. If a pixel is non-zero, it is included in the perimeter and connected to at least one zero-valued pixel. Therefore, the edges of interior holes are considered part of the object's perimeter. Figure 25 shows the segmentation results and identifies the edges of the iced transmission line.

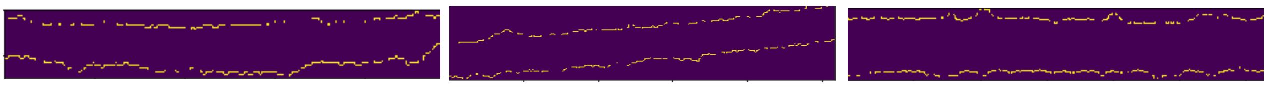

(**a**) (**b**) (**c**)

Figure 25. The edges of the iced transmission line. (**a**) Image 1; (**b**) Image 2; (**c**) Image 3.

5.2.7. The Recognition of Transmission Line Icing

At this stage, the contours of the transmission line icing area are identified. The top and bottom lines of the iced transmission line were determined in advance for further analysis of the binocular vision scheme using 3D measurements. Thus, labeling is needed to recognize independent objects. In this study, connected component labeling is used to distinguish between upper and lower boundary areas, or right and left. Figure 26 shows the edge-extracted images and the images identified at the top and bottom of the line icing.

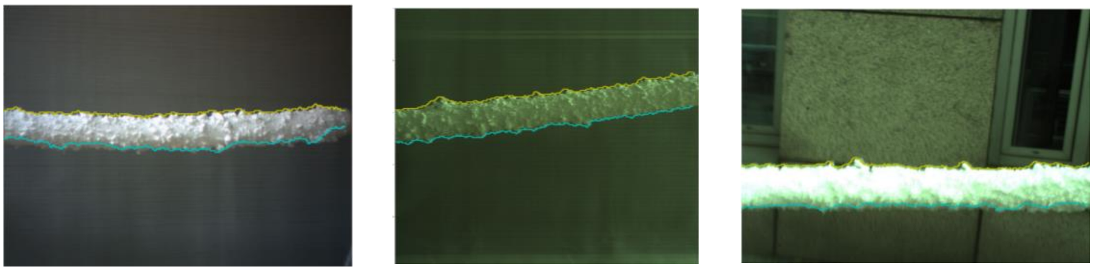

(**a**) (**b**) (**c**)

Figure 26. The images after identifying the top and bottom lines of the line icing. (**a**) Image 1; (**b**) Image 2; (**c**) Image 3.

5.3. Verification and Analysis

Each image that becomes the test data will be marked with the edge of the iced transmission line by ground truth (expert labeling).

System testing involves comparing the expert labeling results with our proposed scheme. By comparing the test image that an expert manually generated with the image that our proposed method detected, it is possible to determine the value of the confusion matrix component. The image will be converted into binary form. Then, the number of pixels detected by our proposed scheme will be known as the actual transmission line icing area by applying the AND operator. Transmission line icing will be marked with a binary value of 1, and non-line icing will be marked with a binary value of 0. Confusion matrix validation is used in the performance testing of our proposed scheme. Figure 27 is an example of comparing ground truth detection results to our proposed scheme detection results. The experiments in this paper used test images from 50 images taken randomly. The confusion matrix results from 50 PTLI images based on the experiment are shown in Table 4.

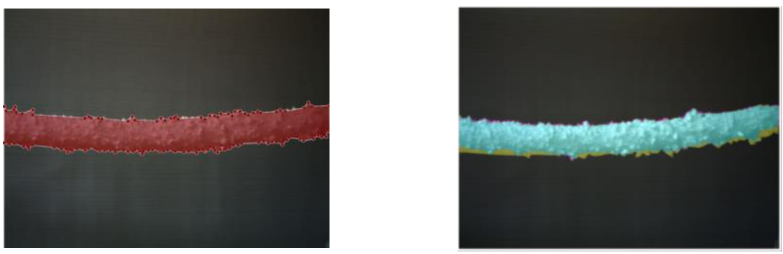

(**a**) (**b**)

Figure 27. The evaluation image of the (**a**) ground truth image testing and the (**b**) proposed method.

Table 4. Confusion matrix from 50 PTLI images.

Accuracy	Recall	Specificity	Precision
0.9771	0.9624	0.8622	0.9948

Based on the result of the evaluation matrix for validation of our proposed scheme, the accuracy value is 97.71%, the precision value is 96.24%, the recall value is 86.22%, and the specificity value is 99.48%. Generally, our proposed scheme is reliable for PTLI images with complex backgrounds and images with poor lighting. Another advantage of this scheme is being able to distinguish between objects and backgrounds, making it easier to recognize objects in images with complex backgrounds. Identification of the top and bottom lines has also been successfully conducted by marking a different color between the top and bottom edges to make it easier to measure the thickness of the ice. Therefore, our proposed scheme effectively resolves iced transmission line identification issues and significantly increases automation.

Our proposed scheme, the previous method, and a manual measurement obtained the ice thickness values at specified locations from the three image pairs. In addition, the manual measurement results are measured by a micrometer caliper with an accuracy of 0.05 mm. The previous method used Canny transform for edge detection and the Hough transform for upper and lower line detection [23,24]. Table 5 shows the comparison results in detail. It shows that the mean absolute error is small based on all experiments, so this scheme is acceptable for ice thickness measurement. Assume the actual value of ice thickness is the manually measured value; the average accuracy of our method can reach 90%.

Table 5. The experimental result for ice thickness (mm).

	Location	**1**	**2**	**3**
Experiment 1	Manual measurement (mm)	88.80	81.50	84.1
	Previous method (mm) [23,24]	119.4	92.1	94.5
	Proposed method (mm)	89.5	81.0	85.9
	Absolute Error	0.70	0.56	1.80
	Location	**1**	**2**	**3**
Experiment 2	Manual measurement (mm)	83.2	89.2	86.8
	Previous method (mm) [23,24]	73.8	119.8	91.2
	The proposed method (mm)	73.2	87.5	85.3
	Absolute Error	1.0	1.7	0.5
	Location	**1**	**2**	**3**
Experiment 3	Manual measurement (mm)	90.2	87.8	80.06
	Previous method (mm) [23,24]	120.8	118.4	90.46
	The proposed method (mm)	89.7	87.1	79.1
	Absolute Error	0.5	0.7	1.5

6. Conclusions

This paper proposes a method of line icing identification for PTLI monitoring. In the initial stage, we integrate image restoration techniques with image filter enhancement to restore the image's color information. This combined approach effectively retains valuable information and preserves the original image quality, thereby mitigating noise introduced during the image acquisition. Subsequently, in the second stage, this paper introduced an enhanced multi-threshold algorithm to accurately separate background and target pixels. Through connected component labeling modification and mathematical morphology operations, we improve the image and find the region of interest (ROI) while eliminating the background regions. We apply the proposed method to measure ice thickness in the PTLI scene, and the average accuracy can be up to 90% compared with manual measurement. Based on the result of the evaluation matrix for validation of our proposed scheme, the accuracy value is 97.71%, the precision value is 96.24%, the recall value is 86.22%, and the specificity value is 99.48%. Our proposed scheme is reliable for PTLI images with complex backgrounds, images with poor illumination, and the position of the transmission line. Another advantage of this scheme is being able to distinguish between objects and backgrounds. Identification of the top and bottom lines has also been successfully conducted by marking a different color between the top and bottom lines to make it easier to measure the thickness of the ice. Therefore, this reliable scheme effectively resolves iced transmission line identification issues and significantly increases automation.

Despite good recognition results, the transmission line recognition and extraction algorithm proposed in this paper still needs further research. For example, if the position of the object (the transmission line icing) in the image is visible from end to end, it will be challenging to recognize the upper and lower lines because, in this study, the image used only takes the smallest part of the transmission line icing into consideration. Additionally, the recall or sensitivity in this scheme is only 86%, so further improvement of image segmentation in transmission line icing images is needed. With the continuous development of UAV and multimedia technology, future detection of transmission lines will be more accurate and convenient. Therefore, this study provides insight for future research with video stream information using real scenes.

Author Contributions: The ideas and concepts were carried out in collaboration with all authors. N.R.N. and J.X. conceived and designed the experiments; N.R.N. and X.H. performed the experiments; N.R.N. and J.X. analyzed the data; N.R.N. and J.X. wrote the paper. All authors have read and agreed to the published version of the manuscript.

Funding: This research received no external funding.

Conflicts of Interest: The authors declare no conflict of interest.

References

1. Guo, Q. Research on the Key Technologies of Power Transmission Line Icing 3D Monitoring Based on Binocular Vision; 2018.
2. Weng, B.; Gao, W.; Zheng, W.; Yang, G. Newly Designed Identifying Method for Ice Thickness on High-Voltage Transmission Lines via Machine Vision. *High Volt.* **2021**, *6*, 904–922. [CrossRef]
3. Wang, J.; Wang, J.; Shao, J.; Li, J. Image Recognition of Icing Thickness on Power Transmission Lines Based on the Least Squares Hough Transform. *Energies* **2017**, *10*, 415. [CrossRef]
4. Guo, Q.; Xiao, J.; Hu, X. New Keypoint Matching Method Using Local Convolutional Features for Power Transmission Line Icing Monitoring. *Sensors* **2018**, *18*, 698. [CrossRef] [PubMed]
5. Nusantika, N.R.; Xiao, J.; Hu, X. New Scheme of Image Matching for The Power Transmission Line Icing. In Proceedings of the ICIEA 2022—Proceedings of the 17th IEEE Conference on Industrial Electronics and Applications, Chengdu, China, 16–19 December 2022.
6. Nusantika, N.R.; Hu, X.; Xiao, J. Improvement Canny Edge Detection for the UAV Icing Monitoring of Transmission Line Icing. In Proceedings of the 16th IEEE Conference on Industrial Electronics and Applications, ICIEA 2021, Chengdu, China, 1–4 August 2021.
7. Imai, I. Studies of Ice Accretion. *Res. Snow Ice* **1953**, *1*, 35–44.
8. Farzaneh, M.; Chisholm, W.A. *Insulators for Icing and Polluted Environments*; John Wiley & Sons: Hoboken, NJ, USA, 2009.
9. Dong, B.; Jiang, X.; Yin, F. Development and Prospect of Monitoring and Prevention Methods of Icing Disaster in China Power Grid. *IET Gener. Transm. Distrib.* **2022**, *16*, 4480–4493. [CrossRef]
10. Zhang, Z.; Zhang, H.; Yue, S.; Zeng, W. A Review of Icing and Anti-Icing Technology for Transmission Lines. *Energies* **2023**, *16*, 601. [CrossRef]
11. Jiang, X.; Xiang, Z.; Zhang, Z.; Hu, J.; Hu, Q.; Shu, L. Predictive Model for Equivalent Ice Thickness Load on Overhead Transmission Lines Based on Measured Insulator String Deviations. *IEEE Trans. Power Deliv.* **2014**, *29*, 1659–1665. [CrossRef]
12. Ma, G.M.; Li, C.R.; Quan, J.T.; Jiang, J.; Cheng, Y.C. A Fiber Bragg Grating Tension and Tilt Sensor Applied to Icing Monitoring on Overhead Transmission Lines. *IEEE Trans. Power Deliv.* **2011**, *26*, 2163–2170. [CrossRef]
13. Zarnani, A.; Musilek, P.; Shi, X.; Ke, X.; He, H.; Greiner, R. Learning to Predict Ice Accretion on Electric Power Lines. *Eng. Appl. Artif. Intell.* **2012**, *25*, 609–617. [CrossRef]
14. Wachal, R.; Stoezel, J.S.; Peckover, M.; Godkin, D. A Computer Vision Early-Warning Ice Detection System for the Smart Grid. In Proceedings of the IEEE Power Engineering Society Transmission and Distribution Conference, Orlando, FL, USA, 7–10 May 2012.
15. Lu, J.Z.; Zhang, H.X.; Fang, Z.; Li, B. Application of Self-Adaptive Segmental Threshold to Ice Thickness Identification. *High Volt. Eng.* **2009**, *35*, 563–567.
16. Gu, I.Y.H.; Berlijn, S.; Gutman, I.; Bollen, M.H.J. Practical Applications of Automatic Image Analysis for Overhead Lines. In Proceedings of the IET Conference Publications, Stockholm, Sweden, 10–13 June 2013.
17. Hao, Y.; Liu, G.; Xue, Y.; Zhu, J.; Shi, Z.; Li, L. Wavelet Image Recognition of Ice Thickness on Transmission Lines. *High Volt. Eng.* **2014**, *40*, 368–373. [CrossRef]

18. Zhang, Y.; Wang, Y.; Wei, A. A New Image Detection Method of Transmission Line Icing Thickness. In Proceedings of the 2020 IEEE 4th Information Technology, Networking, Electronic and Automation Control Conference, ITNEC 2020, Chongqing, China, 12–14 June 2020; pp. 2059–2064. [CrossRef]
19. Xin, G.; Jin, X.; Xiaoguang, H. On-Line Monitoring System of Transmission Line Icing Based on DSP. In Proceedings of the 2010 5th IEEE Conference on Industrial Electronics and Applications, Taichung, Taiwan, 15–17 June 2010; pp. 186–190. [CrossRef]
20. Qi, L.; Wang, J.; Li, C.D.; Liu, W. Research on the Image Segmentation of Icing Line Based on NSCT and 2-D OSTU. *Int. J. Comput. Appl. Technol.* **2018**, *57*, 112–120. [CrossRef]
21. Hemalatha, R.; Rasu, R.; Santhiyakumari, N.; Madheswaran, M. Comparative Analysis of Edge Detection Methods for 3D-Common Carotid Artery Image Using LabVIEW. In Proceedings of the IEEE Conference on Emerging Devices and Smart Systems, ICEDSS 2018, Tiruchengode, India, 2–3 March 2018.
22. Canny, J.F. A Computational Approach to Edge Detection. *IEEE Trans. Pattern Anal. Mach. Intell.* **1986**, *PAMI-8*, 679–698. [CrossRef]
23. Guo, Q.; Hu, X. Power Line Icing Monitoring Method Using Binocular Stereo Vision. In Proceedings of the 2017 12th IEEE Conference on Industrial Electronics and Applications, ICIEA 2017, Siem Reap, Cambodia, 18–20 June 2017.
24. Liu, Y.; Tang, Z.; Xu, Y. Detection of Ice Thickness of High Voltage Transmission Line by Image Processing. In Proceedings of the 2017 IEEE 2nd Advanced Information Technology, Electronic and Automation Control Conference, IAEAC 2017, Chongqing, China, 25–26 March 2017.
25. Gayathri Monicka, S.; Manimegalai, D.; Karthikeyan, M. Detection of Microcracks in Silicon Solar Cells Using Otsu-Canny Edge Detection Algorithm. *Renew. Energy Focus* **2022**, *43*, 183–190. [CrossRef]
26. Lu, Y.; Duanmu, L.; Zhai, Z.J.; Wang, Z. Application and Improvement of Canny Edge-Detection Algorithm for Exterior Wall Hollowing Detection Using Infrared Thermal Images. *Energy Build.* **2022**, *274*, 112421. [CrossRef]
27. Jobson, D.J.; Rahman, Z.U.; Woodell, G.A. A Multiscale Retinex for Bridging the Gap between Color Images and the Human Observation of Scenes. *IEEE Trans. Image Process.* **1997**, *6*, 965–976. [CrossRef] [PubMed]
28. Zhang, Z. A Flexible New Technique for Camera Calibration. *IEEE Trans. Pattern Anal. Mach. Intell.* **2000**, *22*, 1330–1334. [CrossRef]